Synthesis of Fluorine Doped Lithium Argyrodite Solid Electrolytes for Solid-State Lithium Metal Batteries

William Arnold,[a] Varun Shreyas,[a] Yang Li,[a,b] Milinda Kalutara Koralalage,[c] Jacek Jasinski,[b] Arjun Thapa[b] Gamini Sumanasekera,[c] Anh T. Ngo,[d,e] Badri Narayanan,[a*] Hui Wang[a,b*]

[a.] Department of Mechanical Engineering Department, University of Louisville, 332 Eastern Parkway, Louisville, KY 40292, USA

[b.] Conn Center for Renewable Energy Research, University of Louisville, 216 Eastern Parkway, Louisville, KY 40208, USA

[c.] Department of Physics & Astronomy, University of Louisville, 102 Natural Science Building, Louisville, KY 40292, USA

[d.] Materials Science Division, Argonne National Laboratory, 9700 S. Cass Avenue, Lemont, IL 60439, USA

[e.] Department of Chemical Engineering, University of Illinois Chicago, 929 W. Taylor St, MC 110, Chicago, IL 60607, USA

[*]Corresponding authors: hui.wang.1@louisville.edu; badri.narayanan@louisville.edu

Abstract

Solid-state lithium batteries (SSLBs) utilizing novel solid electrolytes (SEs) have garnered much attention due to their potential to yield safe and high-energy density batteries. Sulfide-based argyrodite-class SEs are an attractive option due to their impressive ionic conductivity. Recent studies have shown that LiF at the interface between Li and SE enhances electrochemical stability. However, synthesis of F-doped argyrodites has remained challenging due to the high temperatures used in state-of-the-art solid-state synthesis methods. In this work, for the *first* time, we report F-doped $Li_{5+y}PS_5F_y$ argyrodites with tunable doping content and dual dopants (F^-/Cl^- and F^-/Br^-) that were synthesized through a solvent-based approach. Among all compositions, $Li_6PS_5F_{0.5}Cl_{0.5}$ exhibits the highest Li-ion conductivity of 3.5×10^{-4} S cm^{-1} at room temperature. Furthermore, Li symmetric cells using $Li_6PS_5F_{0.5}Cl_{0.5}$ show the best cycling performance amongst the tested cells. X-ray photoelectron spectroscopy and *ab initio* molecular dynamics simulations revealed that the enhanced interfacial stability of $Li_6PS_5F_{0.5}Cl_{0.5}$ SE against Li metal can be attributed to the formation of a stable SEI containing conductive species (Li_3P), alongside LiCl and LiF. These findings open new opportunities to develop high-performance SSLBs using a novel class of F-doped argyrodite electrolytes.

Key Words: Lithium argyrodites; Fluoride dopant; Synthesis; Interface; Solid Electrolytes

1. Introduction

Rechargeable battery technologies that offer high-energy-density, long cycle-life and safety are urgently needed to meet the growing energy storage demands for the electrification of road transport.[1] State-of-the-art lithium ion batteries (LIBs) for electric vehicles (EVs) employ flammable liquid electrolytes, which pose significant safety concerns.[2,3] This has sparked numerous investigations into alternative solutions that offer high safety without compromising on energy density.[4–8] Among these, a particularly lucrative technology is the solid-state Li metal battery (SSLMB), wherein, flammable liquid electrolytes are replaced by solid-state superionic Li-conductors (called solid electrolytes or SEs). Rapid advancements in high-performance ASSLBs requires the development of SEs that exhibit (a) high Li^+ ion conductivity at room temperature ($>10^{-4}$ S cm^{-1}),[9] and (b) good interfacial stability with both Li-metal anodes and cathodes.[4] Additionally, developing simple, economic, and scalable approaches for SE synthesis is vital to bringing ASSLBs to the EV marketplace.[10]

Several sulfides,[11,12] oxides,[13,14] and polymers[15,16] have been proposed as promising SE chemistries for use in ASSLBs. Of these, sulfide SEs exhibit high Li^+ ion conductivity due to the high polarizability of sulfide ions.[17] In particular, much attention has been given to lithium argyrodites such as Li_7PS_6 and halide-doped Li_6PS_5X (X = Cl, Br, I) whose tetrahedral structure allows for the high mobility of Li ions within the atomic framework.[18–20] Alternatively, other anion dopants (i.e. Ge, Sn, Si) have been reported to further increase the ionic conductivity of argyrodite structured solid electrolytes.[21] For Li_6PS_5X SEs, Cl/Br doping not only increases the ionic conductivity, but also improves the argyrodite's electrochemical stability against the Li anode due to the formation of reductive decomposition products (e.g., Li_3P, LiBr/LiCl and Li_2S) at the solid electrolyte interphase (SEI) layer.[4,22–24]

The presence of LiF in the SEI layer has been reported to stabilize the SE/Li anode interface[24–30] and has the potential to provide a wider electrochemical window for sulfide SEs.[24,31] Typically, LiF is incorporated into the SEI layer by introducing additional Li salt additives; this increases the complexity of processing and lacks precise compositional control. From a synthesis standpoint, a more desirable approach would be to directly prepare F-doped argyrodite electrolytes. While such efforts have been devoted to doping Li_7PS_6 with Cl, Br, and I,[4,23] research on the synthesis of fluoride (F)-doped argyrodites (i.e. Li_6PS_5F) remains in its infancy. Zhao et al. had reported to synthesize $Li_6PS_5Cl_{0.3}F_{0.7}$ via solid-state methode,[32] and found that the excellent cycling stability of symmetric cells were attributable to a high concentration of LiF within the argyrodite structure. However, solid-state synthesis methods are both energy and time consuming, typically requiring long periods of ball-milling and heat treatments of ≥550 °C. One way to address this issue is to employ a solvent-based synthesis method that requires much lower temperatures (≤200 °C); such liquid-phase methods have been reported to produce high purity argyrodite SEs (Li_7PS_6 and Li_6PS_5X; X = (Cl, Br, I)).[10,12,33]

Herein, for the *first* time, we demonstrate the synthesis of F-doped argyrodites $Li_6PS_5F_y$ and hybrid-doped $Li_6PS_5F_{0.5}Cl_{0.5}$ and $Li_6PS_5F_{0.5}Br_{0.5}$ SEs *via* a simple, fast, and scalable solvent-based approach. Effects of F-doping on the crystal structure, phase purity, and conductivity of doped lithium argyrodites were studied. In addition, the interfacial reactivity of F-doped argyrodites towards Li metal in symmetric cells was investigated using X-ray photoelectron spectroscopy (XPS) and *ab-initio* molecular dynamics (AIMD) simulation. The results show that $Li_6PS_5F_{0.5}Cl_{0.5}$ holds the highest ionic conductivity of 3.5×10^{-4} S cm^{-1} at room temperature and the lowest activation energy (0.32 eV). Furthermore, $Li_6PS_5F_{0.5}Cl_{0.5}$ also displays the best stability against Li anode due to the synergistic effects of two halogen ions (Cl^- and F^-) at the interface, and the presence of reduced species with good Li^+ ion conductivity (namely Li_3P). This work provides a concrete demonstration of the use of solvent-based synthesis methods to explore new SEs with tunable composition, which will contribute to the development of novel SE materials for the development of ASSLBs.

2. Experimental

2.1 Materials Synthesis

A solvent-based method was employed to synthesize F-doped lithium argyrodites, and the details were described in previous reports.[10,33] Briefly, the reactants of lithium sulfide (Li_2S, Alfa Aesar®), lithium fluoride (LiF, Alfa Aesar), and β-Li_3PS_4 precursor with stoichiometric ratios were dissolved in ethanol solvent and stirred for 1 h at RT in glovebox (argon atmosphere, O_2 and H_2O < 1ppm). The solvent was evaporated, and the remaining product was heated and kept for 1h at 200 °C under vacuum. $Li_{5+y}PS_5F_y$ samples with differing amounts of F doping content were prepared by tuning the molar ratios of LiF to Li_2S (y = 0.1, 0.2, 0.5, 1.0, and 2.0) following the given chemical reaction (Eq. 1). Similarly, dual-doped $Li_6PS_5F_{0.5}X_{0.5}$ (X = Cl and Br) samples were synthesized by mixing the lithium halides using molar ratios for Li_2S:LiF:LiCl (or LiBr) of 1.0:0.5:0.5, as shown in the chemical reaction at Eq. 2.

$$yLiF + Li_2S + Li_3PS_4 \rightarrow Li_{5+y}PS_5F_y \quad \textit{(Eq.1)}$$

$$0.5LiF + 0.5LiX + Li_2S + Li_3PS_4 \rightarrow Li_6PS_5F_{0.5}X_{0.5} \quad \textit{(Eq.2)}$$

2.2 Structural Characterizations

For $Li_{5+y}PS_5F_y$ and $Li_6PS_5F_{0.5}X_{0.5}$ powder samples, X-ray diffraction (XRD, Bruker D8 Discover) was carried out using nickel-filtered Cu-Kα radiation (λ = 1.5418 Å) for phase identification. To calculate phase percentages in the electrolytes, XRD refinement was performed using the GSAS-

II crystallography data analysis software. Raman spectroscopy (Renishaw in Via Raman/PL Microscope) was performed on synthesized samples using a 632.8 nm emission line of a HeNe laser.

2.3 Electrochemical Characterizations

For electrochemical testing, the powder samples were cold pressed into dense pellets (1/2" diameter, ~0.6 mm thick, ~90-92% dense) inside a glovebox under 400 MPa. Electrochemical impedance spectroscopy (EIS) measurements were conducted to evaluate the conductive properties of cold-pressed samples (with C/Al foil on each side) using a Bio-Logic SP300 Potentiostat with an amplitude of 100 mV and a frequency range of 1 MHz to 100 mHz. Additionally, Arrhenius plots were obtained via the combination of EIS measurement with a temperature-controlled chamber from RT to 90 °C. Li|SE|Li symmetric cells were assembled in 2032-coin cells and tested under different current densities (0.05, 0.1, 0.15 mA cm^{-2}) using a Bio-Logic VSP. After cycling, the symmetric cells were disassembled for XPS analysis (Thermo VG Scientific) to study the interface. All electrolyte preparation and cell assembly/disassembly took place inside a glovebox filled with Ar (O_2, H_2O<1ppm). The electrochemical performance of F-doped argyrodite electrolytes was tested in full cells of $LiFePO_4$ (LFP)|SE|Li. To prepare the cathode, LFP powder, PVDF and Super P with weight ratio of 80:10:10 were mixed in N-methylpyrrolidone (NMP) to form a homogeneous slurry, which was subsequently coated on an aluminum foil. The prepared cathode with an active material loading of ~2 mg cm^{-2} was dried at 120 ^{o}C. Prior to battery cycling, trace amounts of nonflammable Pyrrolidinium-based (PYR) ionic liquid with 1M LiTFSI salt was added on both sides of the SE pellet to reduce the resistance from solid/solid contact. Charge and discharge tests were performed over a voltage window of 2.5–4.0 V using 2032-coin cells after the cells were rested for 8 h.

2.4 *Ab initio* Molecular Dynamics Simulations

All the AIMD simulations were performed within the framework of density functional theory (DFT) using projected augmented wave method as implemented in Vienna *Ab initio* Simulation Package (VASP).[34,35] The exchange correlations were described using the Perdew–Burke–Ernzerhof (PBE) functionals[36] within the generalized gradient approximation (GGA) using the pseudopotentials supplied by VASP: Li_sv (valence: $1s^2\ 2s^1\ 2p^0$), P (valence: $3s^2\ 3p^3$), S (valence: $3s^2\ 3p^4$), Cl (valence: $3s^2\ 3p^5$), and F (valence: $2s^2\ 2p^5$). The energy cut off for plane wave basis-set is set at 500 eV. A Gaussian smearing of 0.05 eV was employed to treat the partial electron occupancies for each orbital. The Brillouin zone was sampled at the Γ point only. An energy convergence tolerance of 1×10^{-5} eV was employed for self-consistent field cycles. For geometry relaxation, the atomic coordinates and the lattice parameters were optimized such that the force on each atom was lower than 0.05 eV/Å.

The computational supercell consisted of symmetric Li||SE||Li slabs (with dimensions ~10 Å × 10 Å × 45 Å), in which both Li and SEs were oriented such that their crystallographic [001] directions were aligned normal to the interface, similar to previous works.[37] Three SEs were considered in this study, namely, $Li_6PS_5F_{0.5}Cl_{0.5}$, Li_6PS_5F, and Li_6PS_5Cl. To prepare the Li|SE|Li slab, we employed the following steps: 1) Unit cells of body-centered cubic Li, and SEs were first optimized, (2) thereafter, the optimized unit cells were employed to prepare two 3×3×3 Li (001) slab and a 1×1×2 Li_6PS_5X (001) slab; X = Cl, F or $F_{0.5}Cl_{0.5}$; and (3) these slabs were then stacked in the direction of the surface normal to achieve a symmetric Li|SE|Li slab. The as-prepared slab model was then optimized. Note the supercell sizes were chosen to ensure that the epitaxial strain between Li (001) and Li_6PS_5X is < 1% along any directions within the plane of the interface. Next, we performed AIMD simulations using the optimized slab model to track the evolution of the interface between Li and SEs at the atomic scale. All the AIMD simulations were performed within a canonical ensemble (NVT) at 300 K for 20 ps using a timestep of 1 fs. Constant temperature conditions were maintained using a Nosé-Hoover thermostat as implemented in VASP. Atomic charges for selected snapshots along the AIMD trajectories were calculated using the Bader partitioning scheme.[38,39] To identify the extent of reduction of P and S atoms, we employed threshold values for Bader charges[37] based on the Bader charge values in the pristine electrolyte (corresponding to un-reduced state), and that in the fully reduced forms (P:Li_3P; S:Li_2S). For details on the thresholds and Bader charge ranges corresponding to different reductive states (full, partial, or not) please see Table S3.

3. Results and Discussion

3.1 Structural and Ion Transport Behavior of $Li_{5+y}PS_5F_y$ Electrolytes

Using a solvent-based synthesis method, $Li_{5+y}PS_5F_y$ argyrodites with varying F content (y = 0.1, 0.2, 0.5, 1.0, and 2.0) were prepared and subjected to XRD for phase identification (*Figure 1a*). All samples show strong characteristic diffraction peaks at 2θ = 25.5°, 30°, and 31.2°, attributing to (220), (311), and (222) planes in the argyrodite crystal (cubic *F-43m* symmetry), respectively. At low F content (y = 0.1 and 0.2), the diffraction patterns of $Li_{5+y}PS_5F_y$ samples are almost identical to the characteristic peaks in Li_6PS_5Cl,[33] suggesting that F atoms fully incorporate into argyrodite crystal structure. With increasing F content ($y \geq 0.5$), new diffraction peaks at 2θ = 38.6° and 65.6° (indexed to LiF[25,27]) start to appear and become stronger. In contrast to the pure argyrodite structure observed for Li_6PS_5Cl,[33] the secondary phase of LiF in $Li_{5+y}PS_5F_y$ ($y \geq 0.5$) indicates low F^- incorporation levels in samples synthesized from a solvent-based approach with low heating temperature (200 °C). Additional LiCl phase was also observed for Li_6PS_5Cl samples when the Cl/P ratio was above 1.5.[33,40] To determine the phase purity and lattice parameters of $Li_{5+y}PS_5F_y$ ($y \geq 0.5$) samples, XRD refinement was undertaken with the results shown in *Fig. S1* and *Table S1*. When y = 1.0, Li_6PS_5F is found to have a lattice parameter of a = 9.889 Å, accompanied by 9.5 wt% of LiF. In contrast, when the same doping content is used for Li_6PS_5Cl synthesized through solvent-based methods, pure argyrodite structure is observed.[33] All $Li_{5+y}PS_5F_y$ samples show a strong peak at 421-426 cm^{-1} in their Raman spectra (*Figure 1b*). This frequency range corresponds to the stretching vibration of the P–S bond in PS_4^{3-} (ortho-thiophosphate), as reported by previous studies on argyrodite electrolytes (Li_7PS_6, Li_6PS_5Br and Li_6PS_5Cl).[22,41] The slight shifts in Raman spectra across the different $Li_{5+y}PS_5F_y$ samples are related to the substitution of S^{2-} anions by F^- anions at the S1 (16*e*) site; PS_4^{3-} tetrahedra arrange into hexagonal cages connected *via* the interstitial anion site in argyrodites.[42]

Figure 1c displays the Nyquist plots of $Li_{5+y}PS_5F_y$ samples at room temperature. The resistance R is used to calculate the Li^+ conductivity following the equation of $\sigma = \frac{L}{RA}$, where σ is ionic conductivity, L is the thickness of the cold-pressed pellet, and A is the cross-sectional area of the pellet. $Li_{5+y}PS_5F_y$ (y = 0.1, 0.2) samples show poor ionic conductivity of ~10^{-5} S cm^{-1} despite exhibiting pure argyrodite structure. Since halide anions replace S^{-2} anions in the crystal structure at either the 4a or 4d sites, and the argyrodite's conductivity is dependent on the unequal sharing of these sites to create a disordered pathway for Li^{+1} ions,[44] it is reasonable then to assume that LiF will first occupy these sites in such a way as to create an ordered crystal structure that prevents lithium intercage diffusion. Significant improvements in ionic conductivity are observed for slightly higher doping contents ($y \geq 0.5$), which creates the necessary disorder required for Li-ion movement. The highest Li-ion conductivity of 2.3 $\times 10^{-4}$ S cm^{-1} is achieved by Li_6PS_5F, which contains a small amount of LiF. The enhanced conductivity despite the presence of a secondary phase is similar to previous observations in Cl-rich Li_6PS_5Cl argyrodite.[33,40] Nevertheless, excessive LiF content reduces Li^+ ion conductivity due to the lithium salt's intrinsically poor conductivity (10^{-9} S cm^{-1}).[43] Arrhenius plots in *Figure 1d* show the temperature dependence of Li^+ conductivity for $Li_{5+y}PS_5F_y$ samples following a linear relationship. The activation energies are calculated according to the equation $\sigma = \sigma_0 e^{\frac{-E_a}{RT}}$, and results for different compositions are displayed in *Fig. S2*. Among $Li_{5+y}PS_5F_y$ samples, Li_6PS_5F possesses the lowest activation energy of ~0.45 eV, which is slightly higher than the 0.4 eV displayed by liquid synthesized Li_6PS_5Cl argyrodite.[33]

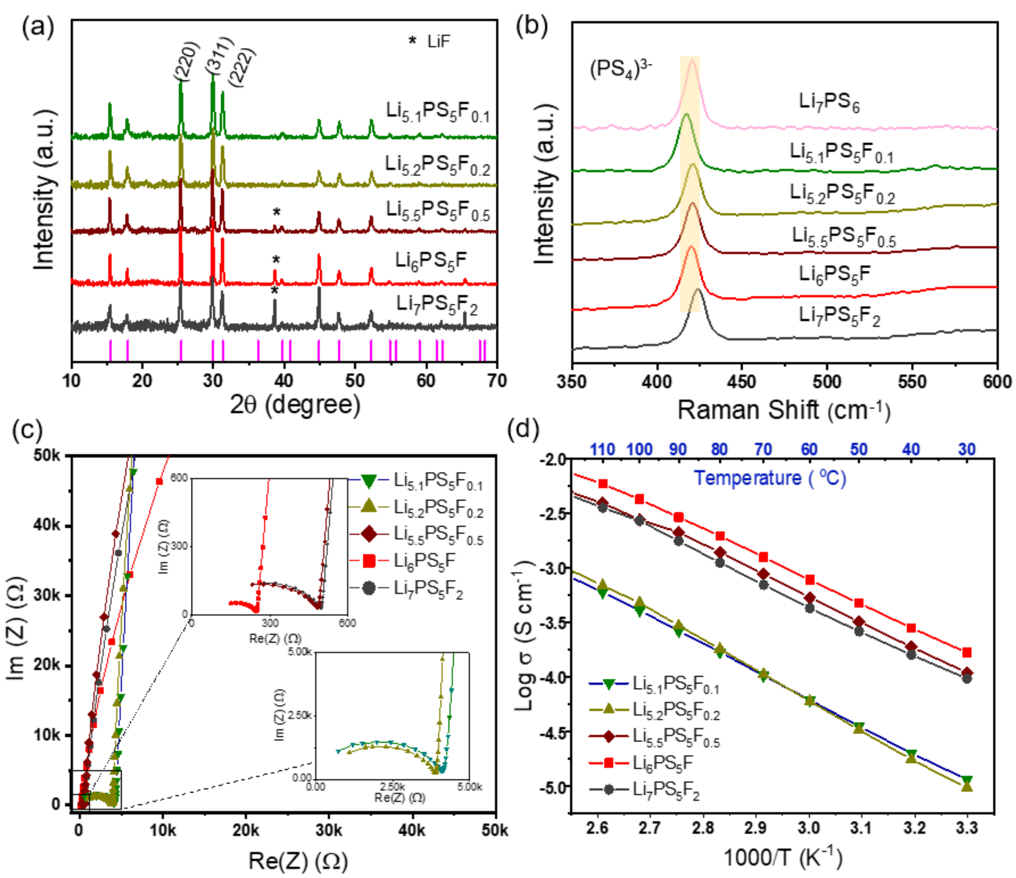

Figure 1. (a) XRD patterns, (b) Raman spectra, (c) Nyquist plots, and (d) Arrhenius plots of F-incorporated lithium argyrodites $Li_{5+y}PS_5F_y$ (y = 0.1, 0.2, 0.5, 1, 2) that were synthesized from a solvent-based method.

3.2 Synthesis and Characterization of Hybrid Halide Doped $Li_6PS_5F_{0.5}X_{0.5}$ Argyrodites

In addition to single-halogen doping (i.e., F^-), $Li_6PS_5F_{0.5}X_{0.5}$ (X = Cl, Br) samples containing two halogen dopants were also synthesized using a solvent-based method. *Figure 2a* presents the XRD pattens for $Li_6PS_5F_{0.5}Cl_{0.5}$ and $Li_6PS_5F_{0.5}Br_{0.5}$ samples, which show characteristic peaks at $2\theta = 25.5^\circ$, 30°, 31.2°, corresponding to the (220), (311), and (222) planes in the argyrodite structure. These diffraction peaks are in excellent accordance with that for Li_7PS_6 and Li_6PS_5X (X = Cl, Br, I).[33] A small peak at $2\theta = 38.6^\circ$ (indexed to LiF) is still present in $Li_6PS_5F_{0.5}X_{0.5}$ samples. XRD refinement results show that $Li_6PS_5F_{0.5}Cl_{0.5}$ contain 7.9 wt% LiF, slightly lower than that in $Li_6PS_5F_{0.5}$ (8.5 wt%). This comparison suggests that the second halide ion (i.e., Cl^- or Br^-) is beneficial to the incorporation of F^- ions into the argyrodite structure. Raman spectra for $Li_6PS_5F_{0.5}X_{0.5}$ (X = Cl, Br) (*Figure 2b*) samples exhibit an obvious peak at 421-423 cm^{-1} attributed to the stretching vibration of P–S bond in PS_4^{3-}, which is the primary vibrational mode for argyrodite SEs.[33] *Figure 2c* shows the Arrhenius plots of $Li_6PS_5F_{0.5}X_{0.5}$ (X = Cl, Br) and Li_6PS_5F from room temperature to 110 °C. $Li_6PS_5F_{0.5}Cl_{0.5}$ sample exhibits the lowest activation energy of 0.32 eV while also possessing the highest ionic conductivity of 3.5×10^{-4} S cm^{-1} at room temperature (*Figure 2d*), followed closely by $Li_6PS_5F_{0.5}Br_{0.5}$ at 3.2×10^{-4} S cm^{-1}. Both $Li_6PS_5F_{0.5}Cl_{0.5}$ and $Li_6PS_5F_{0.5}Br_{0.5}$ have faster ion transport properties than those solvent-synthesized argyrodites with single dopants, i.e., Li_6PS_5X (X = Cl, Br),[10,33,45] and Li_6PS_5F (2.3 $\times10^{-4}$ S cm^{-1}).

Table S2 displays a large variety of argyrodite SEs synthesized from different methods: solid-state, solvent-based, and hybrid.[46–51] In general, the solid-state synthesis approach—which requires extensive ball-milling high temperature heat treatment (~550 °C)—yields argyrodites with the fastest Li-ion transport.[47,52] For the hybrid synthesis method, the starting materials are mixed in solvents and finished by the high temperature heat treatment (400-550 °C).[48,53] Such heat treatment results in higher ionic conductivity of hybrid-synthesized argyrodites than those from solvent-based synthesis method after heated at low temperature (≤200 °C).[15,50,51] In this work, the ionic conductivity of F-doped and dual doped argyrodites SEs falls well within the expected range (~10^{-4} S cm^{-1}) for low-temperature, solvent-based synthesized Li_6PS_5X (X = Cl, Br) argyrodites. Despite relatively lower ionic conductivity, a solvent-based synthesis method with low heating temperature and a short reaction time (1-3 hours) is attractive for practical applications in large-batch synthesis.

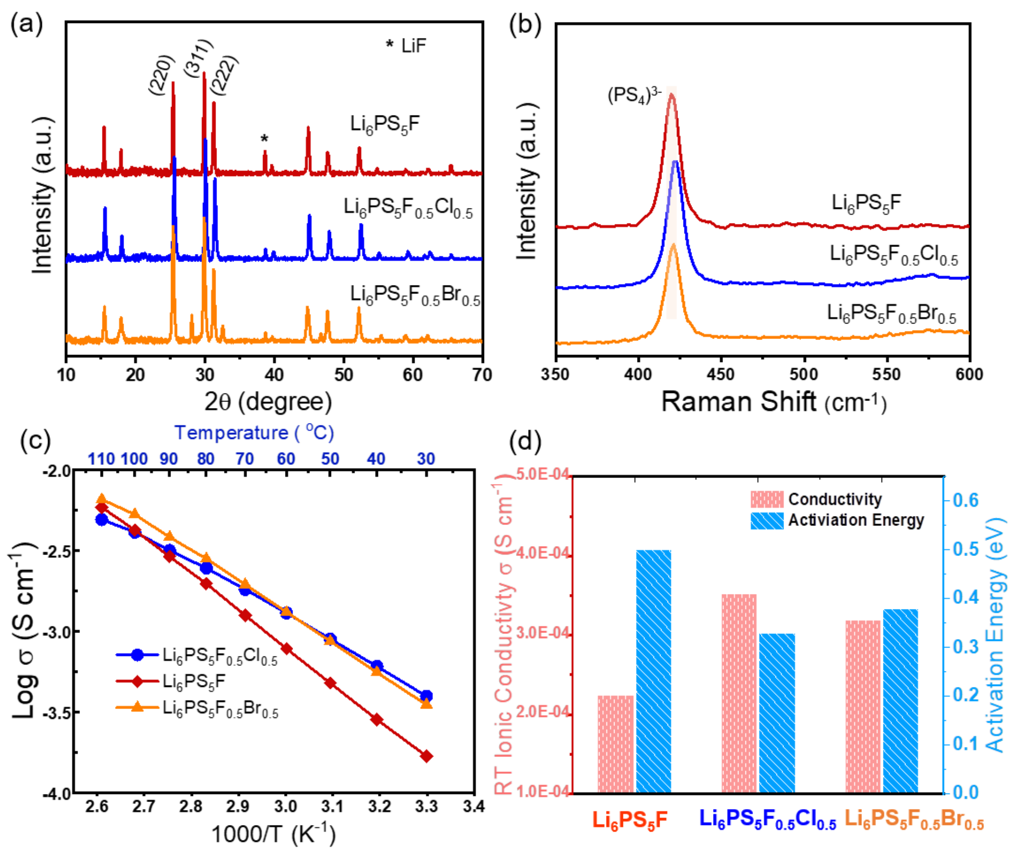

Figure 2. (a) XRD patterns, (b) Raman spectra, (c) Arrhenius plots and (d) RT conductivity/activation energy of $Li_6PS_5F_{0.5}X_{0.5}$ samples (X=Cl, Br), in comparison with Li_6PS_5F.

3.3 Electrochemical Stability in Li Symmetric Cells

Symmetric cells (Li|SE|Li) were assembled and cycled to evaluate the compatibility of F-doped argyrodite SEs ($Li_6PS_5F_{0.5}Cl_{0.5}$ and Li_6PS_5F) towards metallic Li anode. For comparison, Li_6PS_5Cl SE synthesized from solvent-based approach was prepared and confirmed as pure tetragonal phase by XRD patterns and Raman spectrum (*Fig. S3*). Before cycling, the impedance of three symmetric cells shows a decreasing trend of 2200 Ω for Li_6PS_5F, 910 Ω for Li_6PS_5Cl, and 370 Ω for $Li_6PS_5F_{0.5}Cl_{0.5}$. Such discrepancies in the total resistance (R_{total}) of the three symmetric cells is ascribed primarily to different interfacial resistances (R_{int}) present in each cell (*Fig. S4 and Table S3*). *Figure 3a* displays the symmetric cell cycling for three SEs under a low current density of 0.05 mA cm^{-2}, all of which show smooth voltage profiles with polarization voltage values following $Li_6PS_5F_{0.5}Cl_{0.5} < Li_6PS_5Cl < Li_6PS_5F$. When the current density is increased to 0.1 mA cm^{-2} (*Figure 3b*), the Li_6PS_5F-based cell fails first as there is no observable increase in polarization voltage. After cycling for 12 cycles, a sudden voltage drop is observed for the cell with Li_6PS_5Cl SE, which is confirmed to be a short-circuit based on EIS measurement (*Fig. S5*). In contrast, $Li_6PS_5F_{0.5}Cl_{0.5}$-based symmetric cell exhibits stable cycling performance under the same current density (0.1 mA cm^{-2}). After further increasing the current density to 0.15 mA cm^{-2}, the symmetric cell with $Li_6PS_5F_{0.5}Cl_{0.5}$ SE shows flat and stable voltage profiles for over 300 cycles (*Figure 3c*), which indicates stable interface formation between $Li_6PS_5F_{0.5}Cl_{0.5}$ SE and Li anode in the symmetric cells.

Figure 3d shows the XPS spectra of the electrode/electrolyte interface in the $Li_6PS_5F_{0.5}Cl_{0.5}$-based symmetric cell after cycling. Beside strong $(PS_4)^{3-}$ motifs originating from the argyrodite structure, it is observed that the $Li_6PS_5F_{0.5}Cl_{0.5}$ SE undergoes reductive decomposition upon contact with Li metal to form a solid electrolyte interphase (SEI) layer. The best fits for S *2p*, and P *2p* peaks reveal that such an SEI layer in the $Li_6PS_5F_{0.5}Cl_{0.5}$-based cell contains reduced species of P (P_2S_x, Li_3P) and S (Li_2S); the Li *1s* peak fitting suggests the co-presence of LiF and LiCl.[4,54,55] For the two other cycled symmetric cells, reductive species such as P_2S_x, Li_2S, and LiF (or LiCl), are observed at the SE/Li interface, but are notably missing the Li_3P peak at 129.5 eV which is present in the dual-doped SE (*Fig. S6*). Note that although the observation of LiF between Li and Li_6PS_5F, it may not form as a uniform layer, which is typically needed for dendrite suppression. This provides a possible explanation for the cycling failure in the cells with Li_6PS_5F electrolyte while cycling under 0.1 mA/cm^2.

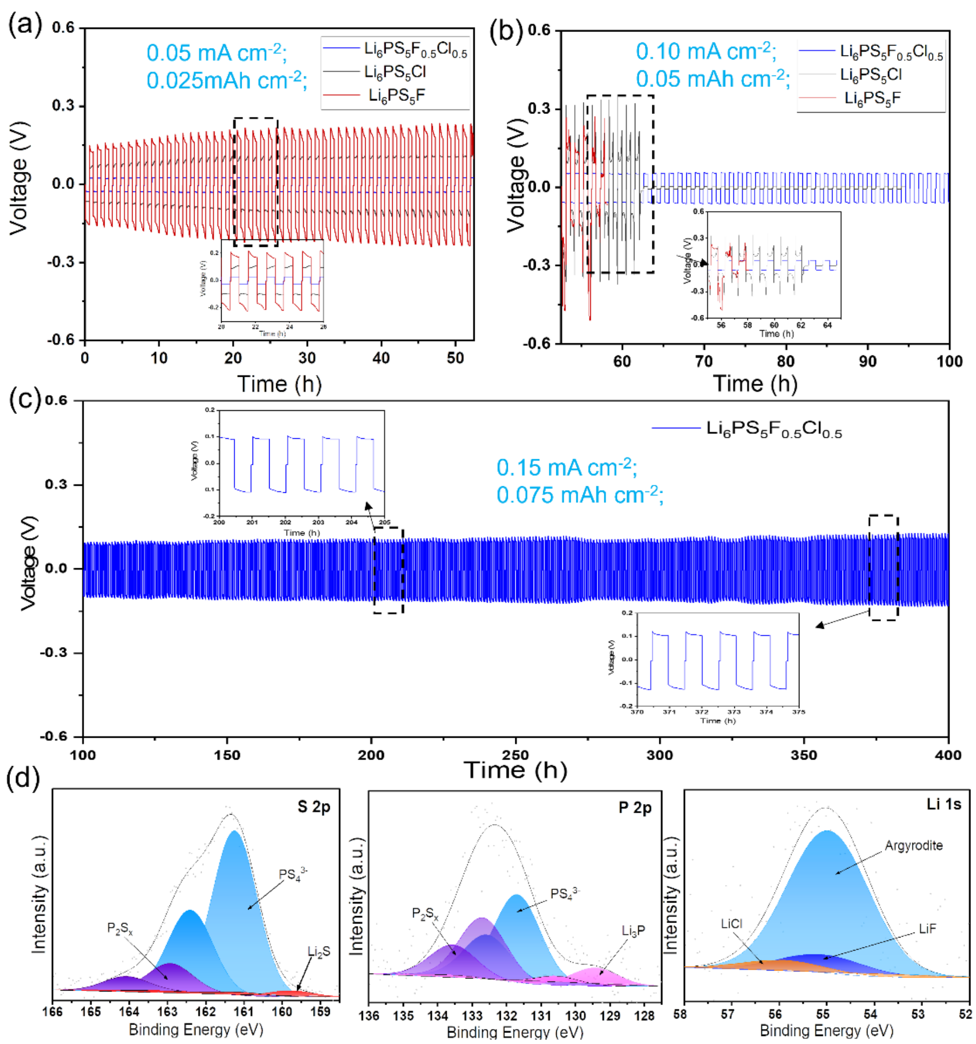

Figure 3. Voltage profiles of Li|SE|Li symmetric cells cycling with three SEs (Li_6PS_5F, Li_6PS_5Cl, $Li_6PS_5F_{0.5}Cl_{0.5}$) under different current densities: (a) 0.05 mA cm^{-2} (0.025mAh cm^{-2}); (b) 0.10 mA cm^{-2} (0.05mAh cm^{-2}) (c) 0.15 mA cm^{-2} (0.075mAh cm^{-2}); charge/discharge for each cycle is 0.5 hour, and (d) XPS spectra of S 2p, P 2p, and Li 1s peaks from the cycled interface of Li symmetric cell using $Li_6PS_5F_{0.5}Cl_{0.5}$ SE.

3.4 Understanding Interfacial Reactions Between Li and F-doped argyrodites by Simulations

To better understand interfacial reactions between Li metal and F-containing argyrodite SEs, we employed a combination of DFT calculations and AIMD simulations. The DFT calculation results show exothermic interfacial energies for three SE against Li metal, in specific, Li|Li_6PS_5F: -0.27 J m^{-2} Li|Li_6PS_5Cl:-0.43 J m^{-2}; Li|$Li_6PS_5F_{0.5}Cl_{0.5}$: -0.34 J m^{-2}. This indicates that interfacial reactions occur between each argyrodite SE and Li metal, which is consistent with previous first-principles works.[37,56]

Figure 4 displays AIMD simulations results to elucidate the atomic-scale details of the structural evolution at the interface between Li metal and three argyrodite SEs ($Li_6PS_5F_{0.5}Cl_{0.5}$ Li_6PS_5F, and Li_6PS_5Cl). Careful analysis of our AIMD trajectories show extensive inter-mixing of atoms between Li-electrode and SEs; for instance, ~5-13% of the Li atoms in the electrode migrate to the SE, while ~8-12 % of S atoms move into electrode from the electrolyte during 20 ps of AIMD simulations (*Figure* 4*(a-f)*). Such intermixing of atoms across the Li-electrolyte interface is accompanied by (*i*) progressive increase in interfacial energy, making it more exothermic (*Fig. S7*), (ii) reduction in average Bader charge on P (up to ~1*e*) and S atoms (up to ~0.25*e*) (*Fig. S9(a-b)*), and (iii) formation of new Li-P, Li-S and Li-X bonds (*Fig. S8(c-e)*), consistent with previous first principles reports.[37,56] Note that these processes occur mainly during the first ~12 ps of the

AIMD simulations for all SEs; thereafter, the systems are largely equilibrated (*Fig. S7, S8*). These processes clearly indicate reductive decomposition of the $Li_6PS_5F_{0.5}Cl_{0.5}$ SE to form a stable SEI.

To identify the interfacial reactions and the composition of the SEI, we classified the P and S atoms in various representative snapshots (at various timesteps) from AIMD trajectories into (i) non-reduced, (ii) partially reduced, (iii) fully reduced states by comparing their calculated Bader charges with that in Li_3P (fully reduced P) and Li_2S (fully-reduced S) and pristine electrolyte (un-reduced P and S) in *Table S4*. For all the SEs, we found that $(PS_4)^{3-}$ motifs in the SEs decompose to form reduced species, namely, $(PS_3)^{2-}$, $(PS_2)^{-}$, PS, Li_3P, and Li_2S. However, the extent of reduction, and the relative fraction of various reaction products depends on the composition of the SE. *Figure 4(g, h)* show the relative fractions of the different reduced states of P and S in the SEI formed with the three electrolytes. We found that SEI associated with all three SEs contain Li_2S (an insulator for Li^+ ions, ~10^{-24} S cm^{-1}). Integrated radial distribution functions (RDF) averaged over the last 3 ps of our AIMD trajectories show ~6.6–6.9 fully-reduced S neighbors around Li, which is close to coordination number (CN) in bulk Li_2S (CN: 8).[37] The fraction of fully-reduced S atoms (i.e., associated with Li_2S) is the least in Li|Li_6PS_5Cl (*Figure 4(h)*), consistent with our XPS measurements (*Fig.S6*). More importantly, the anodic Li atoms that lie in the vicinity of $Li(PS)_x$ species at the interface are largely coordinated with Cl atoms, yielding ~4.5 Li neighbors for each Cl atom (*Figure S9*). These coordinated Li atoms do not react with $Li(PS)_x$ species to cause further reduction. Consequently, none of the P atoms get fully reduced to Li_3P in the Li|Li_6PS_5Cl interface (*Figure 4(g)*). On the other hand, F atoms in Li|Li_6PS_5F and Li|$Li_6PS_5F_{0.5}Cl_{0.5}$ interfaces prefer to associate themselves with lower number of Li neighbors ~4 (Figure S9). This, in turn, ensures that uncoordinated anodic Li atoms are always available to reduce the $Li(PS)_x$ species at the interface completely, and eventually form Li_3P, which is known to be a good ionic conductor (10^{-2} S/cm) (*Figure 4(g)*). Indeed, integrated RDF between Li and fully-reduced P in the Li|Li_6PS_5F and Li|$Li_6PS_5F_{0.5}Cl_{0.5}$ interfaces averaged over the last 3 ps of AIMD simulations show ~8–9 P neighbors around Li, which is close to CN in Li_3P (11).[37] Note that the fully reduced P atoms in Li|$Li_6PS_5F_{0.5}Cl_{0.5}$ are more negatively charged (Bader charge ~ –2.76 *e*) as compared to that in Li|Li_6PS_5F (Bader charge ~ –2.51 *e*). Furthermore, the Li-coordination around fully reduced P in Li|$Li_6PS_5F_{0.5}Cl_{0.5}$ (CN: ~9) is closer to Li_3P (CN: 11) as compared to that in Li|Li_6PS_5F (CN: ~8). The presence of Li_3P in the SEI can explain the enhanced reduction in interfacial resistance in Li|$Li_6PS_5F_{0.5}Cl_{0.5}$ electrolytes observed in our symmetric cell cycling and XPS spectra (*Figure 3*). Direct visualization of the AIMD trajectories showed that partially reduced P atoms constitute $(PS_x)^{n-}$ species. Integrated RDF analysis suggests the presence of more reduced $(PS_x)^{n-}$ species in the SEI associated with Li|Li_6PS_5Cl (CN: 2.16) as compared to Li|Li_6PS_5F (CN:2.6) and Li|$Li_6PS_5F_{0.5}Cl_{0.5}$ (CN:2.6).

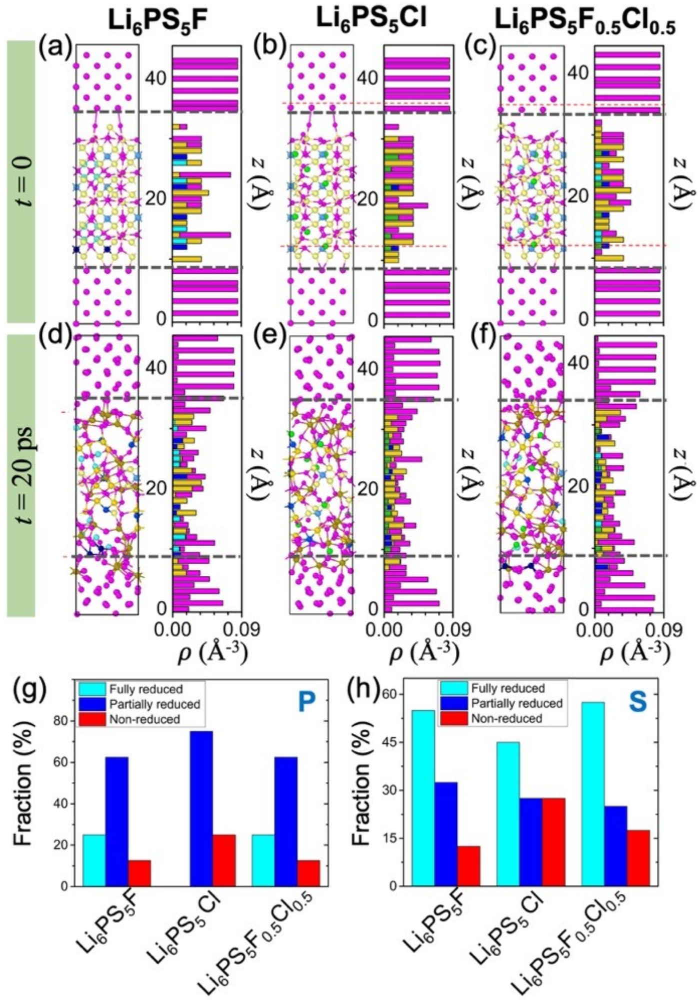

Figure 4. *Ab initio* molecular dynamics simulations of Li (001)| SE (001) | Li (001) interfaces at 300 K. Atomic snapshots (left) and density (ρ) distribution (right) of various atoms across the interfaces for (a) Li_6PS_5F, (b) Li_6PS_5Cl, and (c) $Li_6PS_5F_{0.5}Cl_{0.5}$ at the beginning of the AIMD simulation (t = 0). The corresponding snapshots and density distribution after 20 ps are shown in panels (d-f). Relative fraction of (g) P, and (h) S atoms with different levels of reduction obtained from Bader charge analysis. Fully reduced species for P and S atoms are assumed to be Li_3P and Li_2S respectively; while $(PS_4)^{3-}$ is taken as the non-reduced species. The atoms of Li, P, S, Cl and F are depicted by purple, blue, yellow, green, and cyan spheres. The dotted lines in panels (a-f) indicate the position of the anode.

3.5 Electrochemical Performance in Solid-state Li Batteries that Using $Li_6PS_5F_{0.5}Cl_{0.5}$ SE

Solid-state Li batteries were assembled using $Li_6PS_5F_{0.5}Cl_{0.5}$ as SE, Li metal as the anode, and LFP as the active material in composite cathode and were cycled within the electrochemical window of 2.5-4.0 V. *Figure 5a* shows the cycling performance of the LFP||$Li_6PS_5F_{0.5}Cl_{0.5}$||Li battery under 0.2 C, which has a specific discharge capacity of 122 mAh g^{-1} for the first cycle. The specific discharge capacity further increases to 130 mAh g^{-1} after a few cycles, which is attributed to the formation of an Li_3P-rich and LiF SEI layer; by the 50^{th} cycle, a decent value of 105 mAh g^{-1} has been maintained (*Figure 5b*). The charge/discharge capacity of LFP|$Li_6PS_5F_{0.5}Cl_{0.5}$|Li battery is clearly better than that of the cell using Li_6PS_5Cl (*Fig.S10*), confirming the positive role of F-contained SE. In addition, the C-rate cycling performance of LFP|$Li_6PS_5F_{0.5}Cl_{0.5}$|Li battery under various C-rates (0.2, 0.5, and 0.8 C) is shown in *Figure 5c*. As expected, an obvious specific capacity drop is observed when cycling under higher C-rates, but the battery displays a resumed specific capacity at ~120 mAh g^{-1} after the C-rate is returned to 0.2 C. The great electrochemical performance of $Li_6PS_5F_{0.5}Cl_{0.5}$ SE in LFP||Li cells can be attributed to both the stabilizing effect of F^- and Cl^- from SE, and the adding LiTFSI at the electrode/SE interfaces. Nonetheless, these results demonstrate the excellent potential for F-doped argyrodite SEs to be used in full battery applications.

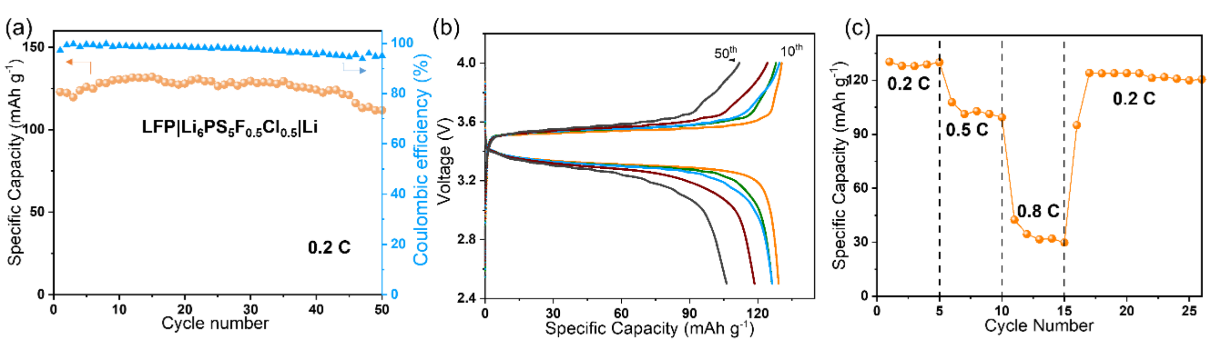

Figure 5. (a) Cycling performance of LFP|$Li_6PS_5F_{0.5}Cl_{0.5}$|Li cell under a current density of 0.2 C; (b) Charge-discharge voltage profiles of LFP||Li cell using $Li_6PS_5F_{0.5}Cl_{0.5}$ SE (voltage window 2.5-4.0V) at 10th, 20th, 30th, 40th and 50th cycles; (c) Rate performance of the cell under various C-rates (0.2 C, 0.5 C, 0.8 C).

4. Conclusion

In summary, for the first time, we reported the synthesis of F-doped lithium argyrodites ($Li_{5+y}PS_5F_y$) and hybrid-doped argyrodites ($Li_6PS_5F_{0.5}Cl_{0.5}$ and $Li_6PS_5F_{0.5}Br_{0.5}$) by a solvent-based approach with low temperature heat treatment. The F-content and hybrid-doped content (F/Cl and F/Br) in argyrodites significantly influences the phase purity and ionic conductive properties. Li_6PS_5F exhibits an impressive conductivity of 2.4 $\times 10^{-4}$ S cm^{-1} while $Li_6PS_5F_{0.5}Cl_{0.5}$ exhibits a higher value of 3.5 $\times 10^{-4}$ S cm^{-1} at room temperature. Moreover, $Li_6PS_5F_{0.5}Cl_{0.5}$ SE shows the best stability towards Li metal in symmetric cells among the tested halide-doped argyrodites. XPS analysis and AIMD simulations reveal that such enhanced stability is attributed to the conductive species (Li_3P), and to the co-presence of LiCl and LiF. The assembled LFP|$Li_6PS_5F_{0.5}Cl_{0.5}$|Li cell displays good cycling performance with a specific discharge capacity above 105 mAh g^{-1} after 50 cycles. This work demonstrates the synthesis of F-doped lithium argyrodites and investigates the interfacial stability of F-doped argyrodites against Li metal, contributing to the development of novel solid electrolytes for use in future solid-state Li batteries.

Acknowledgement

This work was supported by U.S. Department of Energy's Office of Energy Efficiency and Renewable Energy (EERE) Grant under the Vehicle Technologies Office (Award No. DE-

EE0008866). The authors also acknowledge support from the EVPRI Internal Grant at University of Louisville, and Conn Center for Renewable Energy Research. V.S. and B.N acknowledge the resources of the National Energy Research Scientific Computing Center, a DOE Office of Science User Facility supported by the Office of Science of the U.S. Department of Energy under Contract No. DE-AC02-05CH11231. Use of the Center for Nanoscale Materials was supported by the U. S. Department of Energy, Office of Science, Office of Basic Energy Sciences, under Contract No. DE-AC02–06CH11357. A.N. and B.N. also acknowledge the computing resources provided on Bebop, a high-performance computing cluster operated by the Laboratory Computing Resource Center at Argonne National Laboratory.

Supporting Information Description

Additional experimental details are included in the supporting information, including XRD refinement and impedance spectra fitting, comparison of conductive properties of argyrodites from different synthesis method, XPS spectra, and AIMS simulations.

References

(1) Yu, C.; Ganapathy, S.; Eck, E. R. H. van; Wang, H.; Basak, S.; Li, Z.; Wagemaker, M. Accessing the Bottleneck in All-Solid State Batteries, Lithium-Ion Transport over the Solid-Electrolyte-Electrode Interface. *Nat. Commun.* **2017**, *8*. https://doi.org/10.1038/s41467-017-01187-y.

(2) Wang, S.; Zhang, Y.; Zhang, X.; Liu, T.; Lin, Y.-H.; Shen, Y.; Li, L.; Nan, C.-W. High-Conductivity Argyrodite Li6PS5Cl Solid Electrolytes Prepared via Optimized Sintering Processes for All-Solid-State Lithium–Sulfur Batteries. *ACS Appl. Mater. Interfaces* **2018**, *10* (49), 42279–42285. https://doi.org/10.1021/acsami.8b15121.

(3) Tarascon, J.-M. Key Challenges in Future Li-Battery Research. *Philos. Trans. R. Soc. Math. Phys. Eng. Sci.* **2010**, *368* (1923), 3227–3241. https://doi.org/10.1098/rsta.2010.0112.

(4) Tan, D. H. S.; Wu, E. A.; Nguyen, H.; Chen, Z.; Marple, M. A. T.; Doux, J.-M.; Wang, X.; Yang, H.; Banerjee, A.; Meng, Y. S. Elucidating Reversible Electrochemical Redox of Li6PS5Cl Solid Electrolyte. *ACS Energy Lett.* **2019**, *4* (10), 2418–2427. https://doi.org/10.1021/acsenergylett.9b01693.

(5) Chen, M.; Yin, X.; V. Reddy, M.; Adams, S. All-Solid-State MoS 2 /Li 6 PS 5 Br/In–Li Batteries as a Novel Type of Li/S Battery. *J. Mater. Chem. A* **2015**, *3* (20), 10698–10702. https://doi.org/10.1039/C5TA02372F.

(6) Wu, X.; Song, K.; Zhang, X.; Hu, N.; Li, L.; Li, W.; Zhang, L.; Zhang, H. Safety Issues in Lithium Ion Batteries: Materials and Cell Design. *Front. Energy Res.* **2019**, *7*. https://doi.org/10.3389/fenrg.2019.00065.

(7) Cheng, X.-B.; Zhang, R.; Zhao, C.-Z.; Zhang, Q. Toward Safe Lithium Metal Anode in Rechargeable Batteries: A Review. *Chem. Rev.* **2017**, *117* (15), 10403–10473. https://doi.org/10.1021/acs.chemrev.7b00115.

(8) Liu, D.-H.; Bai, Z.; Li, M.; Yu, A.; Luo, D.; Liu, W.; Yang, L.; Lu, J.; Amine, K.; Chen, Z. Developing High Safety Li-Metal Anodes for Future High-Energy Li-Metal Batteries: Strategies and Perspectives. *Chem. Soc. Rev.* **2020**, *49* (15), 5407–5445. https://doi.org/10.1039/C9CS00636B.

(9) Rayavarapu, P. R.; Sharma, N.; Peterson, V. K.; Adams, S. Variation in Structure and Li+-Ion Migration in Argyrodite-Type Li6PS5X (X = Cl, Br, I) Solid Electrolytes. *J. Solid State Electrochem.* **2012**, *16* (5), 1807–1813. https://doi.org/10.1007/s10008-011-1572-8.

(10) Ziolkowska, D. A.; Arnold, W.; Druffel, T.; Sunkara, M.; Wang, H. Rapid and Economic Synthesis of a Li7PS6 Solid Electrolyte from a Liquid Approach. *ACS Appl. Mater. Interfaces* **2019**, *11* (6), 6015–6021. https://doi.org/10.1021/acsami.8b19181.

(11) Rao, R. P.; Adams, S. Studies of Lithium Argyrodite Solid Electrolytes for All-Solid-State Batteries. *Phys. Status Solidi A* **2011**, *208* (8), 1804–1807. https://doi.org/10.1002/pssa.201001117.

(12) Li, Y.; Arnold, W.; Jasinski, J. B.; Thapa, A.; Sumanasekera, G.; Sunkara, M.; Narayanan, B.; Druffel, T.; Wang, H. Interface Stability of LiCl-Rich Argyrodite Li6PS5Cl with Propylene Carbonate Boosts High-Performance Lithium Batteries. *Electrochimica Acta* **2020**, *363*, 137128. https://doi.org/10.1016/j.electacta.2020.137128.

(13) Dawson, J. A.; Canepa, P.; Clarke, M. J.; Famprikis, T.; Ghosh, D.; Islam, M. S. Toward Understanding the Different Influences of Grain Boundaries on Ion Transport in Sulfide

and Oxide Solid Electrolytes. *Chem. Mater.* **2019**, *31* (14), 5296–5304. https://doi.org/10.1021/acs.chemmater.9b01794.

(14) Zhang, Z.; Shao, Y.; Lotsch, B.; Hu, Y.-S.; Li, H.; Janek, J.; F. Nazar, L.; Nan, C.-W.; Maier, J.; Armand, M.; Chen, L. New Horizons for Inorganic Solid State Ion Conductors. *Energy Environ. Sci.* **2018**, *11* (8), 1945–1976. https://doi.org/10.1039/C8EE01053F.

(15) Kim, D. H.; Lee, Y.-H.; Song, Y. B.; Kwak, H.; Lee, S.-Y.; Jung, Y. S. Thin and Flexible Solid Electrolyte Membranes with Ultrahigh Thermal Stability Derived from Solution-Processable Li Argyrodites for All-Solid-State Li-Ion Batteries. *ACS Energy Lett.* **2020**, *5* (3), 718–727. https://doi.org/10.1021/acsenergylett.0c00251.

(16) Zhang, D.; Xu, X.; Qin, Y.; Ji, S.; Huo, Y.; Wang, Z.; Liu, Z.; Shen, J.; Liu, J. Recent Progress in Organic–Inorganic Composite Solid Electrolytes for All-Solid-State Lithium Batteries. *Chem. – Eur. J.* **2020**, *26* (8), 1720–1736. https://doi.org/10.1002/chem.201904461.

(17) Rao, R. P.; Sharma, N.; Peterson, V. K.; Adams, S. Formation and Conductivity Studies of Lithium Argyrodite Solid Electrolytes Using In-Situ Neutron Diffraction. *Solid State Ion.* **2013**, *230*, 72–76. https://doi.org/10.1016/j.ssi.2012.09.014.

(18) Deiseroth, H.-J.; Maier, J.; Weichert, K.; Nickel, V.; Kong, S.-T.; Reiner, C. Li7PS6 and Li6PS5X (X: Cl, Br, I): Possible Three-Dimensional Diffusion Pathways for Lithium Ions and Temperature Dependence of the Ionic Conductivity by Impedance Measurements. *Z. Für Anorg. Allg. Chem.* **2011**, *637* (10), 1287–1294. https://doi.org/10.1002/zaac.201100158.

(19) Boulineau, S.; Courty, M.; Tarascon, J.-M.; Viallet, V. Mechanochemical Synthesis of Li-Argyrodite Li6PS5X (X=Cl, Br, I) as Sulfur-Based Solid Electrolytes for All Solid State Batteries Application. *Solid State Ion.* **2012**, *221*, 1–5. https://doi.org/10.1016/j.ssi.2012.06.008.

(20) Yu, C.; Ganapathy, S.; Eck, E. R. H. van; Eijck, L. van; Basak, S.; Liu, Y.; Zhang, L.; W. Zandbergen, H.; Wagemaker, M. Revealing the Relation between the Structure, Li-Ion Conductivity and Solid-State Battery Performance of the Argyrodite Li 6 PS 5 Br Solid Electrolyte. *J. Mater. Chem. A* **2017**, *5* (40), 21178–21188. https://doi.org/10.1039/C7TA05031C.

(21) Zhou, L.; Assoud, A.; Zhang, Q.; Wu, X.; Nazar, L. F. New Family of Argyrodite Thioantimonate Lithium Superionic Conductors. *J. Am. Chem. Soc.* **2019**, *141* (48), 19002–19013. https://doi.org/10.1021/jacs.9b08357.

(22) Zhang, J.; Zheng, C.; Li, L.; Xia, Y.; Huang, H.; Gan, Y.; Liang, C.; He, X.; Tao, X.; Zhang, W. Unraveling the Intra and Intercycle Interfacial Evolution of Li6PS5Cl-Based All-Solid-State Lithium Batteries. *Adv. Energy Mater.* **2020**, *10* (4), 1903311. https://doi.org/10.1002/aenm.201903311.

(23) Xu, H.; Yu, Y.; Wang, Z.; Shao, G. A Theoretical Approach to Address Interfacial Problems in All-Solid-State Lithium Ion Batteries: Tuning Materials Chemistry for Electrolyte and Buffer Coatings Based on Li 6 PA 5 Cl Hali-Chalcogenides. *J. Mater. Chem. A* **2019**, *7* (10), 5239–5247. https://doi.org/10.1039/C8TA11151K.

(24) Fan, X.; Ji, X.; Han, F.; Yue, J.; Chen, J.; Chen, L.; Deng, T.; Jiang, J.; Wang, C. Fluorinated Solid Electrolyte Interphase Enables Highly Reversible Solid-State Li Metal Battery. *Sci. Adv.* **2018**, *4* (12), eaau9245. https://doi.org/10.1126/sciadv.aau9245.

(25) Patel, S.; Banerjee, S.; Liu, Y.; Wang, P.; Chien, P.; Feng, X.; Liu, J.; Ong, S.P.; Hu, Y.Y.; Tunable Lithium Ion Transport in Mixed-Halide Argyrodites Li6-xPS5-xClBrx: An Unusual Compositional Space, Chem. Mater., **2021**, 33 (4), 1435-1443.
(26) Han, X.; Sun, J. Design of a LiF-Rich Solid Electrolyte Interface Layer through Salt-Additive Chemistry for Boosting Fast-Charging Phosphorus-Based Lithium Ion Battery Performance. *Chem. Commun.* **2020**, *56* (45), 6047–6049. https://doi.org/10.1039/D0CC01853H.
(27) Kim, H.; Kim, Y. S.; Yoo, J. In Situ Formed LiF Protective Layer on Li Metal Anode with Solventless Cross-Linking. **2020**, 4, 3282-3287.
(28) Cui, C.; Yang, C.; Eidson, N.; Chen, J.; Han, F.; Chen, L.; Luo, C.; Wang, P.-F.; Fan, X.; Wang, C. A Highly Reversible, Dendrite-Free Lithium Metal Anode Enabled by a Lithium-Fluoride-Enriched Interphase. *Adv. Mater.* **2020**, *32* (12), 1906427. https://doi.org/10.1002/adma.201906427.
(29) Zhang, S.; Zhao, F.; Wang, S.; Liang, J.; Wang, J.; Wang, C.; Zhang, H.; Adair, K.; Li, W.; Li, M.; Duan, H.; Zhao, Y.; Yu, R.; Li, R.; Huang, H.; Zhang, L.; Zhao, S.; Lu, S.; Sham, T.-K.; Mo, Y.; Sun, X. Advanced High-Voltage All-Solid-State Li-Ion Batteries Enabled by a Dual-Halogen Solid Electrolyte. *Adv. Energy Mater.* **2021**, *11* (32), 2100836. https://doi.org/10.1002/aenm.202100836.
(30) Yu, T.; Liang, J.; Luo, L.; Wang, L.; Zhao, F.; Xu, G.; Bai, X.; Yang, R.; Zhao, S.; Wang, J.; Yu, J.; Sun, X. Superionic Fluorinated Halide Solid Electrolytes for Highly Stable Li-Metal in All-Solid-State Li Batteries. *Adv. Energy Mater.* **2021**, *11* (36), 2101915. https://doi.org/10.1002/aenm.202101915.
(31) Zhu, Y.; He, X.; Mo, Y. Origin of Outstanding Stability in the Lithium Solid Electrolyte Materials: Insights from Thermodynamic Analyses Based on First-Principles Calculations. *ACS Appl. Mater. Interfaces* **2015**, *7* (42), 23685–23693. https://doi.org/10.1021/acsami.5b07517.
(32) Zhao, F.; Sun, Q.; Yu, C.; Zhang, S.; Adair, K.; Wang, S.; Liu, Y.; Zhao, Y.; Liang, J.; Wang, C.; Li, X.; Li, X.; Xia, W.; Li, R.; Huang, H.; Zhang, L.; Zhao, S.; Lu, S.; Sun, X. Ultrastable Anode Interface Achieved by Fluorinating Electrolytes for All-Solid-State Li Metal Batteries. *ACS Energy Lett.* **2020**, *5* (4), 1035–1043. https://doi.org/10.1021/acsenergylett.0c00207.
(33) Arnold, W.; Buchberger, D. A.; Li, Y.; Sunkara, M.; Druffel, T.; Wang, H. Halide Doping Effect on Solvent-Synthesized Lithium Argyrodites Li6PS5X (X= Cl, Br, I) Superionic Conductors. *J. Power Sources* **2020**, *464*, 228158. https://doi.org/10.1016/j.jpowsour.2020.228158.
(34) Kresse, G.; Furthmüller, J. Efficient Iterative Schemes for Ab Initio Total-Energy Calculations Using a Plane-Wave Basis Set. *Phys. Rev. B* **1996**, *54* (16), 11169–11186. https://doi.org/10.1103/PhysRevB.54.11169.
(35) Kresse, G.; Joubert, D. From Ultrasoft Pseudopotentials to the Projector Augmented-Wave Method. *Phys. Rev. B* **1999**, *59* (3), 1758–1775. https://doi.org/10.1103/PhysRevB.59.1758.
(36) Perdew, J. P.; Burke, K.; Ernzerhof, M. Generalized Gradient Approximation Made Simple. *Phys. Rev. Lett.* **1996**, *77* (18), 3865–3868. https://doi.org/10.1103/PhysRevLett.77.3865.

(37) Camacho-Forero, L. E.; Balbuena, P. B. Exploring Interfacial Stability of Solid-State Electrolytes at the Lithium-Metal Anode Surface. *J. Power Sources* **2018**, *396*, 782–790. https://doi.org/10.1016/j.jpowsour.2018.06.092.
(38) Yu, M.; Trinkle, D. R. Accurate and Efficient Algorithm for Bader Charge Integration. *J. Chem. Phys.* **2011**, *134* (6), 064111. https://doi.org/10.1063/1.3553716.
(39) Tang, W.; Sanville, E.; Henkelman, G. A Grid-Based Bader Analysis Algorithm without Lattice Bias. *J. Phys. Condens. Matter* **2009**, *21* (8), 084204. https://doi.org/10.1088/0953-8984/21/8/084204.
(40) Adeli, P.; Bazak, J. D.; Park, K. H.; Kochetkov, I.; Huq, A.; Goward, G. R.; Nazar, L. F. Boosting Solid-State Diffusivity and Conductivity in Lithium Superionic Argyrodites by Halide Substitution. *Angew. Chem. Int. Ed.* **2019**, *58* (26), 8681–8686. https://doi.org/10.1002/anie.201814222.
(41) Zhang, Z.; Zhang, L.; Yan, X.; Wang, H.; Liu, Y.; Yu, C.; Cao, X.; van Eijck, L.; Wen, B. All-in-One Improvement toward Li6PS5Br-Based Solid Electrolytes Triggered by Compositional Tune. *J. Power Sources* **2019**, *410–411*, 162–170. https://doi.org/10.1016/j.jpowsour.2018.11.016.
(42) Zhang, J.; Zheng, C.; Lou, J.; Xia, Y.; Liang, C.; Huang, H.; Gan, Y.; Tao, X.; Zhang, W. Poly(Ethylene Oxide) Reinforced Li6PS5Cl Composite Solid Electrolyte for All-Solid-State Lithium Battery: Enhanced Electrochemical Performance, Mechanical Property and Interfacial Stability. *J. Power Sources* **2019**, *412*, 78–85. https://doi.org/10.1016/j.jpowsour.2018.11.036.
(43) He, M.; Guo, R.; Hobold, G. M.; Gao, H.; Gallant, B. M. The Intrinsic Behavior of Lithium Fluoride in Solid Electrolyte Interphases on Lithium. *Proc. Natl. Acad. Sci.* **2020**, *117* (1), 73–79. https://doi.org/10.1073/pnas.1911017116.
(44) Brinek, M.; Hiebl, C.; Wilkening, H. M. R. Understanding the Origin of Enhanced Li-Ion Transport in Nanocrystalline Argyrodite-Type Li6PS5I. *Chem. Mater.* **2020**, *32* (11), 4754–4766. https://doi.org/10.1021/acs.chemmater.0c01367.
(45) Zhang, Z.; Zhang, L.; Liu, Y.; Yan, X.; Xu, B.; Wang, L. One-Step Solution Process toward Formation of Li6PS5Cl Argyrodite Solid Electrolyte for All-Solid-State Lithium-Ion Batteries. *J. Alloys Compd.* **2020**, *812*, 152103. https://doi.org/10.1016/j.jallcom.2019.152103.
(46) Chen, Y.; Li, W.; Sun, C.; Jin, J.; Wang, Q.; Chen, X.; Zha, W.; Wen, Z. Sustained Release-Driven Formation of Ultrastable SEI between Li6PS5Cl and Lithium Anode for Sulfide-Based Solid-State Batteries. *Adv. Energy Mater.* **2021**, *11* (4), 2002545. https://doi.org/10.1002/aenm.202002545.
(47) Liu, G.; Weng, W.; Zhang, Z.; Wu, L.; Yang, J.; Yao, X. Densified Li6PS5Cl Nanorods with High Ionic Conductivity and Improved Critical Current Density for All-Solid-State Lithium Batteries. *Nano Lett.* **2020**, *20* (9), 6660–6665. https://doi.org/10.1021/acs.nanolett.0c02489.
(48) Zhou, L.; Park, K.-H.; Sun, X.; Lalère, F.; Adermann, T.; Hartmann, P.; Nazar, L. F. Solvent-Engineered Design of Argyrodite Li6PS5X (X = Cl, Br, I) Solid Electrolytes with High Ionic Conductivity. *ACS Energy Lett.* **2019**, *4* (1), 265–270. https://doi.org/10.1021/acsenergylett.8b01997.
(49) Choi, S.; Ann, J.; Do, J.; Lim, S.; Park, C.; Shin, D. Application of Rod-Like Li6PS5Cl Directly Synthesized by a Liquid Phase Process to Sheet-Type Electrodes for All-Solid-

State Lithium Batteries. *J. Electrochem. Soc.* **2018**, *166* (3), A5193. https://doi.org/10.1149/2.0301903jes.
(50) Rosero-Navarro, N. C.; Miura, A.; Tadanaga, K. Composite Cathode Prepared by Argyrodite Precursor Solution Assisted by Dispersant Agents for Bulk-Type All-Solid-State Batteries. *J. Power Sources* **2018**, *396*, 33–40. https://doi.org/10.1016/j.jpowsour.2018.06.011.
(51) Yubuchi, S.; Uematsu, M.; Deguchi, M.; Hayashi, A.; Tatsumisago, M. Lithium-Ion-Conducting Argyrodite-Type Li 6 PS 5 X (X = Cl, Br, I) Solid Electrolytes Prepared by a Liquid-Phase Technique Using Ethanol as a Solvent. *ACS Appl. Energy Mater.* **2018**, *1* (8), 3622–3629. https://doi.org/10.1021/acsaem.8b00280.
(52) Wang, P.; Liu, H.; Patel, S.; Feng, X.; Chien, P.-H.; Wang, Y.; Hu, Y.-Y. Fast Ion Conduction and Its Origin in Li6–XPS5–XBr1+x. *Chem. Mater.* **2020**, *32* (9), 3833–3840. https://doi.org/10.1021/acs.chemmater.9b05331.
(53) Subramanian, Y.; Rajagopal, R.; Ryu, K.-S. High Ionic-Conducting Li-Argyrodites Synthesized Using a Simple and Economic Liquid-Phase Approach and Their Application in All Solid-State-Lithium Batteries. *Scr. Mater.* **2021**, *204*, 114129. https://doi.org/10.1016/j.scriptamat.2021.114129.
(54) Hikima, K.; Phuc, N. H. H.; Tsukasaki, H.; Mori, S.; Muto, H.; Matsuda, A. High Ionic Conductivity of Multivalent Cation Doped Li 6 PS 5 Cl Solid Electrolytes Synthesized by Mechanical Milling. *RSC Adv.* **2020**, *10* (38), 22304–22310. https://doi.org/10.1039/D0RA02545C.
(55) Hanghofer, I.; Brinek, M.; L. Eisbacher, S.; Bitschnau, B.; Volck, M.; Hennige, V.; Hanzu, I.; Rettenwander, D.; R. Wilkening, H. M. Substitutional Disorder: Structure and Ion Dynamics of the Argyrodites Li 6 PS 5 Cl, Li 6 PS 5 Br and Li 6 PS 5 I. *Phys. Chem. Chem. Phys.* **2019**, *21* (16), 8489–8507. https://doi.org/10.1039/C9CP00664H.
(56) Yubuchi, S.; Uematsu, M.; Hotehama, C.; Sakuda, A.; Hayashi, A.; Tatsumisago, M. An Argyrodite Sulfide-Based Superionic Conductor Synthesized by a Liquid-Phase Technique with Tetrahydrofuran and Ethanol. *J. Mater. Chem. A* **2019**, *7* (2), 558–566. https://doi.org/10.1039/C8TA09477B.
(57) Chida, S.; Miura, A.; Rosero-Navarro, N. C.; Higuchi, M.; Phuc, N. H. H.; Muto, H.; Matsuda, A.; Tadanaga, K. Liquid-Phase Synthesis of Li6PS5Br Using Ultrasonication and Application to Cathode Composite Electrodes in All-Solid-State Batteries. *Ceram. Int.* **2018**, *44* (1), 742–746. https://doi.org/10.1016/j.ceramint.2017.09.241.
(58) Yu, C.; Li, Y.; Li, W.; Adair, K. R.; Zhao, F.; Willans, M.; Liang, J.; Zhao, Y.; Wang, C.; Deng, S.; Li, R.; Huang, H.; Lu, S.; Sham, T.-K.; Huang, Y.; Sun, X. Enabling Ultrafast Ionic Conductivity in Br-Based Lithium Argyrodite Electrolytes for Solid-State Batteries with Different Anodes. *Energy Storage Mater.* **2020**, *30*, 238–249. https://doi.org/10.1016/j.ensm.2020.04.014.
(59) Wang, H.; Yu, C.; Ganapathy, S.; van Eck, E. R. H.; van Eijck, L.; Wagemaker, M. A Lithium Argyrodite Li6PS5Cl0.5Br0.5 Electrolyte with Improved Bulk and Interfacial Conductivity. *J. Power Sources* **2019**, *412*, 29–36. https://doi.org/10.1016/j.jpowsour.2018.11.029.

(60) Auvergniot, J.; Cassel, A.; Foix, D.; Viallet, V.; Seznec, V.; Dedryvère, R. Redox Activity of Argyrodite Li6PS5Cl Electrolyte in All-Solid-State Li-Ion Battery: An XPS Study. *Solid State Ion.* **2017**, *300*, 78–85. https://doi.org/10.1016/j.ssi.2016.11.029.

(61) Wenzel, S.; Sedlmaier, S. J.; Dietrich, C.; Zeier, W. G.; Janek, J. Interfacial Reactivity and Interphase Growth of Argyrodite Solid Electrolytes at Lithium Metal Electrodes. *Solid State Ion.* **2018**, *318*, 102–112. https://doi.org/10.1016/j.ssi.2017.07.005.
(62) Cheng, T.; Merinov, B. V.; Morozov, S.; Goddard, W. A. Quantum Mechanics Reactive Dynamics Study of Solid Li-Electrode/Li6PS5Cl-Electrolyte Interface. *ACS Energy Lett.* **2017**, *2* (6), 1454–1459. https://doi.org/10.1021/acsenergylett.7b00319.

Table of Content Graphic

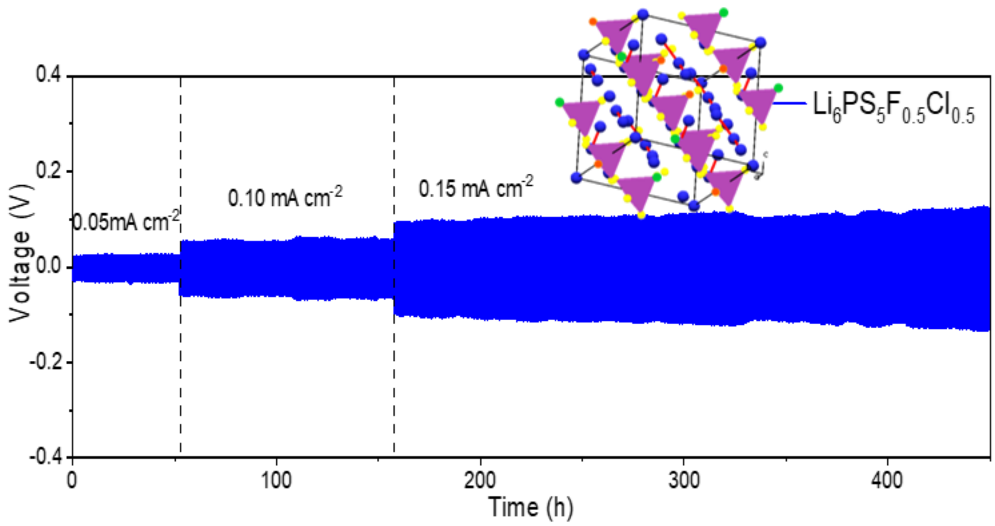

Florine (F)-contained argyrodites with tunable doping content and dual dopants (F^-/Cl^- and F^-/Br^-) have been reported to synthesize via a solvent-based approach. Among them, $Li_6PS_5F_{0.5}Cl_{0.5}$ SE exhibits the highest ionic conductivity and the best interface stability against Li anode.